Article

Detection of Large-Scale Floods Using Google Earth Engine and Google Colab

Rosa Johary * , Christophe Révillion , Thibault Catry , Cyprien Alexandre , Pascal Mouquet ,
Solofoarisoa Rakotoniaina , Gwenaëlle Pennober , Solofo Rakondraompiana

Posted Date: 20 September 2023

doi: 10.20944/preprints202309.1375.v1

Keywords: flood; radar imagery; Sentinel-1; Google Earth Engine; Python doi:10.20944/preprints202309.1375.v1

Article

Detection of Large-Scale Floods Using Google Earth Engine and Google Colab

Rosa Johary [1,*], Christophe Révillion [2], Thibault Catry [2], Cyprien Alexandre [2], Pascal Mouquet [2], Solofoarisoa Rakotoniaina [1], Gwenaelle Pennober [2] and Solofo Rakotondraompiana [1]

[1] Institut et Observatoire de Géophysique d'Antananarivo – Université d'Antananarivo,101 Antananarivo ; Madagascar ; rosa.johary@univ-antananarivo.mg (R.J.) ; solofoarisoa.rakotoniaina@univ-antananarivo.mg (Sa.R.), solofo.rakotondraompiana@univ-antananarivo.mg (S.R.)
[2] UMR 228 Espace Dev, Univ Montpellier, IRD, Univ Antilles, Univ Guyane, Univ Reunion, IRD Montpellier, France ; pascal.mouquet@ird.fr (P.M.) ; christophe.revillion@univ-reunion.fr (C.R.) ;
* Correspondence: Correspondence: rosa.johary@univ-antananarivo.mg

Abstract: This paper presents an operational approach for detecting floods and establishing flood extent using Sentinel-1 radar imagery with Google Earth Engine. Flooded areas are identified using a change-detection method based on the normalized difference. The HAND algorithm is used to delineate zones for processing. The approach was tested and calibrated at small scale to identify optimal parameters for flood detection. It was then applied to the whole of the island of Madagascar after the cyclone Batsirai in 2022. The proposed method is enabled by the computing power and data availability of Google Earth Engine and Google Colab. The results show satisfactory accuracy in delineating flooded areas. The advantages of this approach are its rapidity, online availability and ability to detect floods over a wide area. The approach relying on Google tools thus offers an effective solution for generating a large-scale synoptic picture to inform hazard management decision-making. However, one of the method's drawbacks is that it depends to a large extent on frequent radar imagery being available at the time of flood events and on free access to the platform. These drawbacks will need to be taken into account in an operational scenario.

Keywords: flood; radar imagery; Sentinel-1; Google Earth Engine; Python

---

1. Introduction

Extreme precipitation events are increasing in frequency and intensity in a number of regions of the globe, driven by climate change [1]. These disruptions in precipitation patterns have consequences on the distribution of water areas, as well as their spatiotemporal dynamics, at various scales. Having knowledge about availability and distribution of water resources is extremely important in order to facilitate their management in the context of climate change. In particular, flooding is on the increase in many countries [2], potentially leaving some 1.81 billion people exposed to a risk of 100-year floods [3]. In Madagascar and the islands in the western Indian Ocean, these problems are compounded by cyclones [4]. While the number of cyclones in the Indian Ocean is not rising, their impacts are increasingly severe [5] and further amplified in developing nations through lack of land planning and reliable and accessible data to inform decisions [6]. Thanks to the increased availability of Earth observation data and the proliferation of different types of images (optical, radar, etc.), satellite imagery has proven to be a valuable tool for continuously mapping the distribution and dynamics of water bodies on a large scale. It also helps quickly identify large-scale flooded areas, aids in disaster relief planning, and contributes to damage quantification in the event of a cyclonic event [7].

Flood map products are generated by a range of international organizations depending on the severity of specific cyclone events. ESA's rapid mapping products are one example [8]. They are usually obtained at the request of local authorities and/or through the International Charter Space and Major Disasters [9]. The FAO also produces flood maps for assessing food security [10]. However, these maps only cover relatively localized areas hit by major cyclones and not all territories affected by flooding. This level of event coverage justifies the need for other larger mapping products at the scale of the affected territories.

Because floods are accompanied by dense cloud cover, the utility of optical remote sensing approaches is nevertheless limited. Indeed, optical remote sensing can lead to an under-estimation of flood extents due to the lack of timely cloud-free satellite imagery to coincide with cyclone events [11]. Earth imaging systems like Landsat 8 and 9 or Sentinel-2 are therefore strongly constrained. Furthermore, intertropical zones are subject to frequent cloud cover. Radar satellite imagery offers a way around this issue, as the wavelengths in radar imagery are on the order of a centimeter, so the atmosphere is almost transparent to them [12].

A flood is an uncommon body of standing water. Such surface water is detected by radar data because backpropagation radar waves from the water surface are much weaker than from other surfaces [13–15]. However, radar imaging systems are also sensitive to surface roughness and the dielectric properties of the surface [16]. It is also possible that the radar response from a standing water surface and a smooth soil surface will be similar. Moreover, side view radar systems can create shadows in imagery. Comparing two radar images acquired before and during or just after a flood happened enables low backscatter features and permanent water bodies to be filtered out [15].

Image comparison supports flood analysis and can be done using supervised or unsupervised [17,18] change detection algorithms [19,20]. It can be done using pixel by pixel simple algebraic operations like subtraction [21], ratio or textural indices [22]. Comparisons can also be operated on previously identified features [23]. The ratio between two images attenuates the speckle effect in radar images [24]. Machine learning is also increasingly used in this field [25]. Phase information from each pixel can also be used to identify changes. Interferometric coherence has been employed to detect floodwaters in urban areas [26].

A digital elevation model (DEM) and water flow properties can improve flood detection by masking and reducing areas to be processed. For this we use topographic indices like the geomorphic flood index (GFI) [27] or height above nearest drainage (HAND) [28]. Razafipahatelo et al. [29] used HAND index to define preferred samples for non-supervised classification. The ever-increasing volume of radar data and the sometimes very wide extent of floods justify this need to bound processing and radar images could take a long time to download depending on available data rates.

Cloud computing services offer a way around these issues. Since Google Earth Engine (GEE) has come on stream [30], a growing number of applications have been developed to use this service for remote sensing and geographic information systems. GEE is a cloud-based geospatial analysis platform that allows users to visualize and analyze Earth-observation (EO) data. GEE's database includes all freely accessible satellite imagery and is refreshed daily. Imagery can be processed directly in the cloud without the need to download it [30] which is very useful in countries like Madagascar where bandwidth can be low and downloading heavy data complicated. GEE is used in a wide range of applications like vegetation mapping and monitoring, land cover mapping, agriculture and hazard management [31,32], including for floods [33].

GEE is accessible via two client libraries. The first one is based on JavaScript (JS) programming language and the second on Python. While both libraries provide access to the same services, Python makes it easy to automate execution of laborious and multiple tasks. This advantage afforded by Python enables parallel processing of several images. Google Colab, an online Python interpreter, is the tool used with GEE's Python application programming interface (API).

In this paper, we report on the development of an image processing chain for identifying floods from several Sentinel-1 scenes. This chain is implemented in Google Colab using the Python API. It was first tested and calibrated on the immediate outskirts of Antananarivo (Madagascar) using optical and radar images acquired before and after a series of floods in 2018. It is then applied to the whole of Madagascar after the passage of Cyclone Batsirai on 5 and 6 February 2022.

The second part of the paper presents the data used for the two applications and the area where calibration was done. We also explain the approach used for the test and calibration phase, as well as the processing chain itself. Then we present and compare our results with other flood maps available during the passage of Cyclone Batsirai, and against results obtained with another processing chain called S1Chain [34]. We also present how results are made available to hazard and disaster management agencies.

2. Materials and Methods

2.1. Study zones

We have developed and calibrated our processing chains to detect flooded areas throughout Madagascar, which is located in the south-west of the Indian Ocean.

To calibrate the processing chain, it was applied first on the plain in the immediate outskirts of Antananarivo, in the center of the island following the passage of Cyclone Ava between January 5th and 9th, 2018.

Our chain was then tested during the passage of the Batsirai cyclone. Cyclone Batsirai swept across southern Madagascar on 5 and 6 February 2022 (Figure 1). Several zones along the island's eastern seaboard were declared disaster areas. Reference flood maps are available for a few zones [8,10].

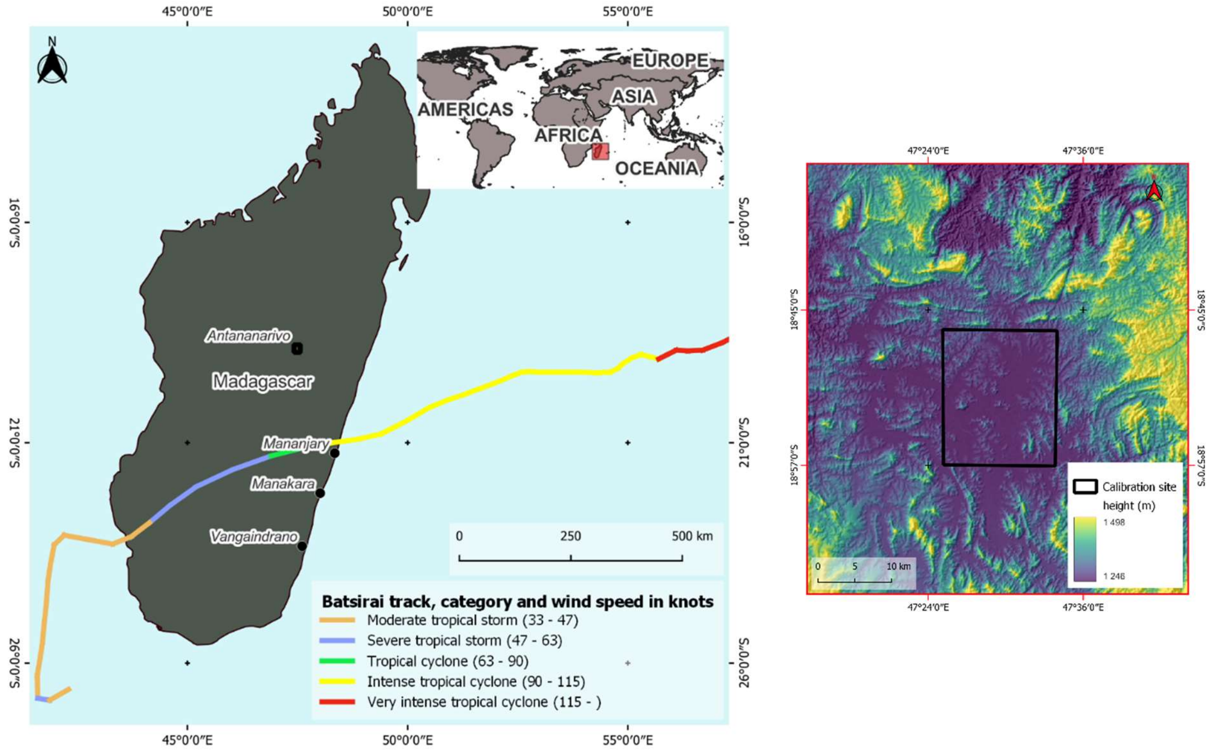

(a) (b)

Figure 1. (a) Track of Cyclone Batsirai as it barreled across southern Madagascar from North-East to South-West on 5 and 6 February 2022. *Source: Track of Cyclone Batsirai, NCEI [35]*; **(b)** Calibration site. To the west of Antananarivo is a plain covered in rice fields that is regularly flooded during the rainy season and especially during cyclones.

2.2. Data

The Sentinel-1 constellation operated by the European Space Agency (ESA) is composed of two satellites, Sentinel-1A and Sentinel-1B. Sentinel-1B ceased operating in July 2022 [36]. The native spatial resolution of Sentinel-1 imagery depends on the satellite's acquisition mode, of which there are four: Stripmap (SM), Interferometric Wide (IW), Extra Wide (EW) and Wave (WV). The respective spatial resolutions for these acquisition modes are 5x5 m, 5x20 m, 20x40 m and 5x5 m.

Sentinel-1 imagery is acquired every 5 to 12 days depending on where the territory being imaged is and on ESA's satellite tasking plans. Unfortunately, these plans do not support emergency retasking [36]. For Madagascar, past and planned acquisition scenarios show that images are acquired by Sentinel-1A in IW mode during the descending phase of its orbit, except for southwest Madagascar where scenes are regularly acquired on two ascending passes. Data are available in both VV and VH polarizations and at least every 12 days. It takes 4 to 10 days to acquire images covering all of Madagascar.

The Sentinel-1 data we used are already stored in GEE. Only GRD (Ground Range Detected) products are available in GEE. In this format, Sentinel-1 image pixels are square—5x5m, 10x10m or 25x25m maximum depending on acquisition mode—and noise is attenuated at the price of coarser resolution and loss of phase information. GEE performs pre-processing on the Sentinel-1 imagery after refreshing the orbit metadata before posting online to suppress edge noise and thermal noise, and to perform radiometric calibration and terrain correction. In the latter case, SRTM 30m digital elevation model data are used [37].

Images available in GEE are stored at several levels of resolution in pyramid mode. The pyramid is built from the original image at its native resolution (base of the pyramid). The next level is formed by combining pixels in groups of four and averaging them. This operation is repeated until an image no larger than 256 x 256 pixels (apex of the pyramid) is obtained. The pyramid level used by GEE for processing is determined automatically by the specified output spatial resolution (display or export) [38]. This enables processing of a vast zone at optimal resolution and avoids overwhelming GEE's computing capacity. However, it is also possible to specify the desired spatial resolution, and while exporting from the JS and Python libraries is possible, automating multiple exports is easier with Python, as each export operation in Javascript in GEE's IDE requires interaction with the user. To streamline the computation without sacrificing too much information, 20-meter resolution images were used.

During the beginning of 2018, there was abundant rainfall in the area around Antananarivo up to the beginning of March, flooding low-lying zones around the city. In March, the rainfall was driven by a tropical depression and then Cyclone Dumazile. On 13 March 2018, good weather conditions enabled a Sentinel-2 optical image with only 1% cloud cover to be acquired, while a Sentinel-1 image is available for 12 March 2018. This Sentinel 2 image and another Sentinel-2 image acquired during the dry season were used to delineate the flooded areas and calibrate processing for Sentinel-1 data. Sentinel-2 images have a native spatial resolution of 10 m, 20 m or 60 m depending on the spectral band. The bands used—visible and near-infrared—offer a resolution of 10 m. In Sentinel-2 images, water surfaces are detected by thresholding the NDWI (Normalized Difference Water Index) with Otsu algorithm [39]. The same method is applied to the reference image to detect and filter out permanent surface waters. The results thus obtained are compared to the processing of radar images.

To simulate a calculation covering the entire territory of Madagascar, flood detection is extended over a 12-day period. This approach aims to ensure complete coverage of the territory using Sentinel images, as the revisit frequency of Sentinel-1 satellites is every 12 days. To ensure a significant presence of flooding, the period following the passage of Cyclone Batsirai on February 5th and 6th, 2022, is chosen. 30 Sentinel-1 scenes were required. They were acquired between 5 and 17 February 2022. Radar images acquired at the same period as these post-flood images for each previous year were used as reference images.

During Batsirai, partial flood maps were produced by the FAO for the island's eastern seaboard and the Copernicus EMRS program for certain zones. Partial flood maps were also produced by the FAO [10] for the island's eastern seaboard and the Rapid Mapping component of the Copernicus Emergency Management Service (CEMS) program for certain zones. The CEMS Rapid Mapping product is a mapping solution tailored for rapid disaster response [8]. It leverages advanced Earth observation satellites (TerraSar-X data) to deliver near real-time, high-resolution satellite imagery and geospatial data during crucial early phases of emergencies like earthquakes, floods, and wildfires. CEMS Rapid Mapping empowers authorities and first responders to quickly assess damage, identify affected areas, and coordinate targeted relief efforts. This rapid access to precise mapping data enhances situational awareness and accelerates aid delivery, bolstering community resilience and safety. Those products were compared to the results obtained by our processing chain for the same zones.

For further validation, the results of the processing chain were compared to the results of the S1Chain developed by Alexandre et al. [34]. This processing chain downloads and extracts Sentinel-1 imagery within the Sentinel-2 tile footprints, incorporates multi-temporal filtering, calculates the normalized difference ratio, and generates a mask delineating flooded regions. The data used was processed following the passage of cyclone Batsirai in 2022, using the same Sentinel-1 data that we processed for this cyclone event. This makes it possible to compare the different chain outputs.

In order to provide practical and rapid information to risk managers, data from European Space Agency (ESA) World Cover [40], OpenStreetMap (OSM) [41] and Google Open Buildings [42] were employed. The ESA World Cover product provides a global land cover map for 2021 at 10 m resolution based on Sentinel-1 and Sentinel-2 data. OSM stands as a collaborative, open-source mapping platform, where contributors worldwide crowdsource geographic data. It furnishes comprehensive, cost-free maps applicable across diverse fields, spanning from navigation to urban planning and disaster response. Meanwhile, Google Open Buildings offers building footprints derived from very high-resolution imagery through advanced deep learning algorithms.

2.3. Processing chain

To make everything less compute-intensive, processing will be applied only to flood-prone zones pre-determined according to topography. The processing chain developed here is based on detecting changes between two Sentinel-1 radar images using the normalized difference ratio. Images acquired before floods for reference and images acquired during or after a flood has peaked are required. The choice of imagery will have a significant impact on results. Before attempting to detect flooded areas, it is also crucial to filter out speckle noise from radar images.

2.3.1. Delineating flood-prone areas

Flood proneness can be measured by a topographic index, among them GFI (Geomorphic Flood Index) [27], FSI (Flood Susceptibility Index) [43] or HAND (Height Above Nearest Drainage) [28]. The advantage of the HAND index is that it can be calculated from a DEM without hydrology data. We assume that water in a given pixel flows towards the next downstream pixel following the steepest slope. Any given pixel may receive water from zero, one or several pixels upstream of it. Water can thus accumulate in a pixel, since water can only flow into a single pixel downstream.

To calculate HAND index, the direction of water flow in each pixel is first deduced from the DEM. The water accumulation rate is then calculated for each pixel (the number of upstream pixels feeding water into it). All pixels with a water accumulation rate above a given threshold, called the flow accumulation threshold (FAT), are considered part of the thalweg network. These are valley lines along which water flows and accumulates when it rains. Once all points in the thalweg network are identified, a matrix connecting each pixel in the study zone to the first point in the network receiving water from this specific pixel is established. This connection matrix, combined with the DEM, enables the value of the HAND parameter to be deduced.

The HAND parameter enables a pixel's flood proneness to be determined: the greater the difference in elevation between the pixel and the thalweg network, the less likely it is to be flooded [28]. By applying a threshold to HAND values, we can identify flood-prone areas and mask all pixels outside of them. This threshold must be chosen to maintain a balance between accuracy and performance. If the threshold value is set too high, non-flood-prone zones will be included and thus needlessly slow down processing; too low, and zones genuinely at risk of flooding will be excluded.

A set of HAND values covering the entire globe is already available in GEE (Donchyts et al. [44]) for FAT threshold values of 100 (local drainage basins) and 1,000 (large drainage basins). DEMs used are SRTM (30 m) and Viewfinder Panoramas (90 m) [45] for latitudes above 60 degrees, where SRTM data are lacking.

Preprints (www.preprints.org) | NOT PEER-REVIEWED | Posted: 20 September 2023 doi:10.20944/preprints202309.1375.v1

In the specific case of Madagascar, a HAND threshold value of 5 m and a FAT value of 100 were chosen to include zones already known to have flooded previously. These values were determined on the basis of data on previous floods and local terrain features.

2.3.2. Choice of reference images

Reference images are usually chosen from dates when there were no floods. There are several options when choosing them. We can choose images acquired during the dry season when water levels are at their lowest. However, this can lead to mistaking a stream bed filling up for a flood. We can also choose an image acquired just before the flood event, but in this case the results would only factor in submersions caused by this specific event and could therefore include seasonal rains, which are not strictly speaking floods, or exclude subsequent submersions due to the floods. The best option would be to use radar images acquired when the main stream beds of water courses are full but not overflowing. However, this precise moment may not coincide with a satellite pass.

An alternative approach is employed here for selecting reference images. For a given scene (post-flood image), all available images acquired during the same period in previous years are selected, starting from 2014. To guarantee at least one image for each year, for Sentinel-1 the period is extended to cover the 12 days preceding the event. A flood-detection operation is then applied to the post-flood image and each of these reference images. The results are combined using a majority-voting process to select pixels corresponding to water. This approach excludes zones that are usually under water (permanent water bodies) during the event in question.

2.3.3. Radar image filtering

Mullissa et al. [46] developed a speckle filtering tool in GEE. However, this tool is not available in Google Colab. Therefore, it was rewritten in Python while developing this processing chain. Speckle filter performance is generally assessed by analyzing how much speckle noise is reduced and how well features are preserved in the filtered image [47,48]. Each filter is assessed in terms of the accuracy with which water bodies are detected. Five filters have been incorporated in the processing chain (boxcar, gamma map [49], Lee [50], Lee Sigma [51] and Refined Lee [52]).

2.3.4. Delineating flood extent by change detection

The change-detection method is based on the normalized difference, first used by Coppin and Bauer [53] and subsequently developed by Gianinetto and Villa [54]. It has already been used to establish flood extents [34].

For two images Y1 and Y2, from the same scene but acquired on different dates, the normalized difference between them is given by:

$D = (Y2-Y1) / (Y2+Y1)$

D is between –1 and +1. A value close to 0 indicates no change, while a value near to +/-1 corresponds to a large decrease or increase in the pixel value between the two dates.

As the reflected signal from areas under water is much weaker, the normalized difference will be negative. We can establish a normalized difference threshold value to delineate flooded areas.

2.3.5. Processing chain overview

Figure 2 below shows a simplified overview of the processing chain.

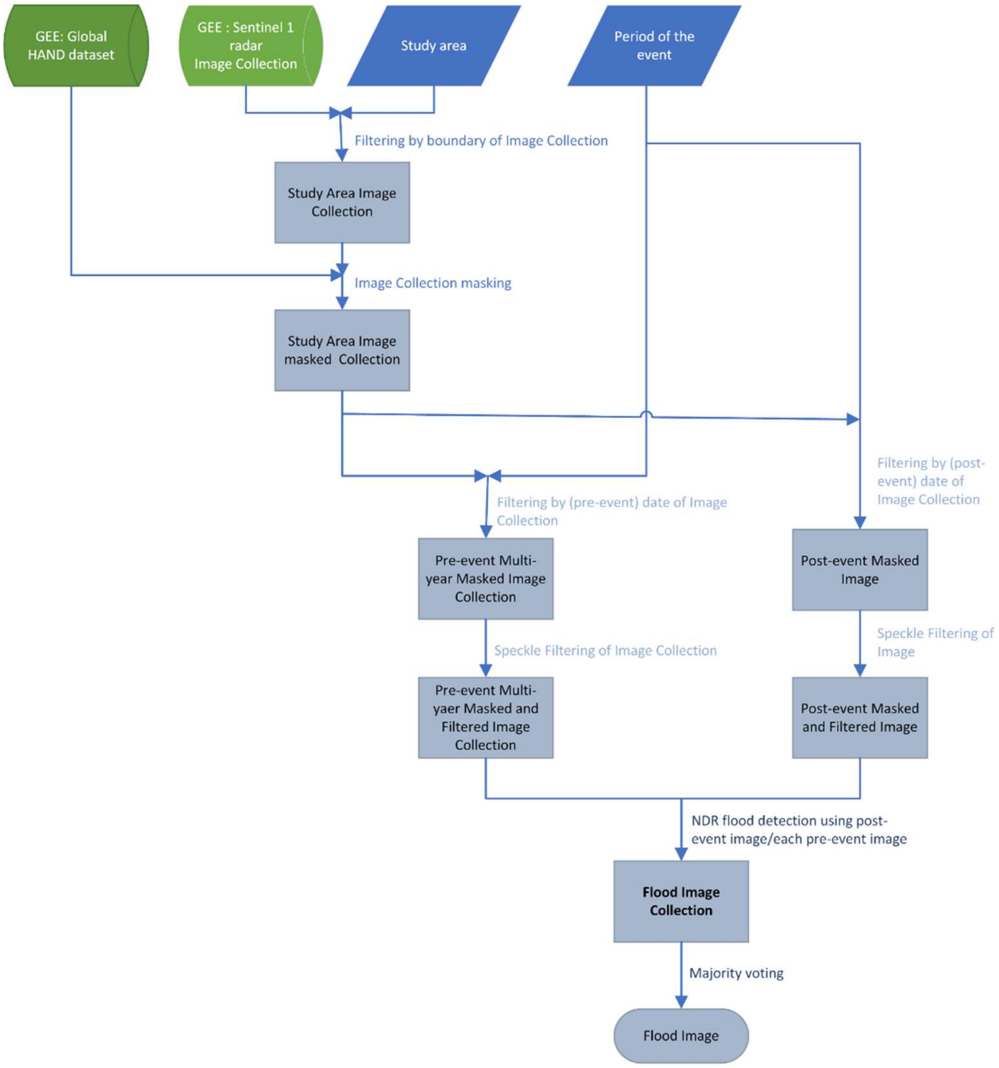

Figure 2. Processing chain overview. GEE: Google Earth Engine, HAND: Height Above Nearest Drainage, NDR: Normalized Difference Ratio.

The processing chain code is freely accessible and commented on Github : https://github.com/johrosa/ls-FloodMonitoring/blob/main/country_scale_flood_detection.ipynb

2.3.6. Calibration and validation of results

To calibrate and assess the effectiveness of the processing chain, the flood-detection protocol was applied to the outskirts of Antananarivo (Figure 3). After comparing results, we choose the best filter and polarizations for flood detection.

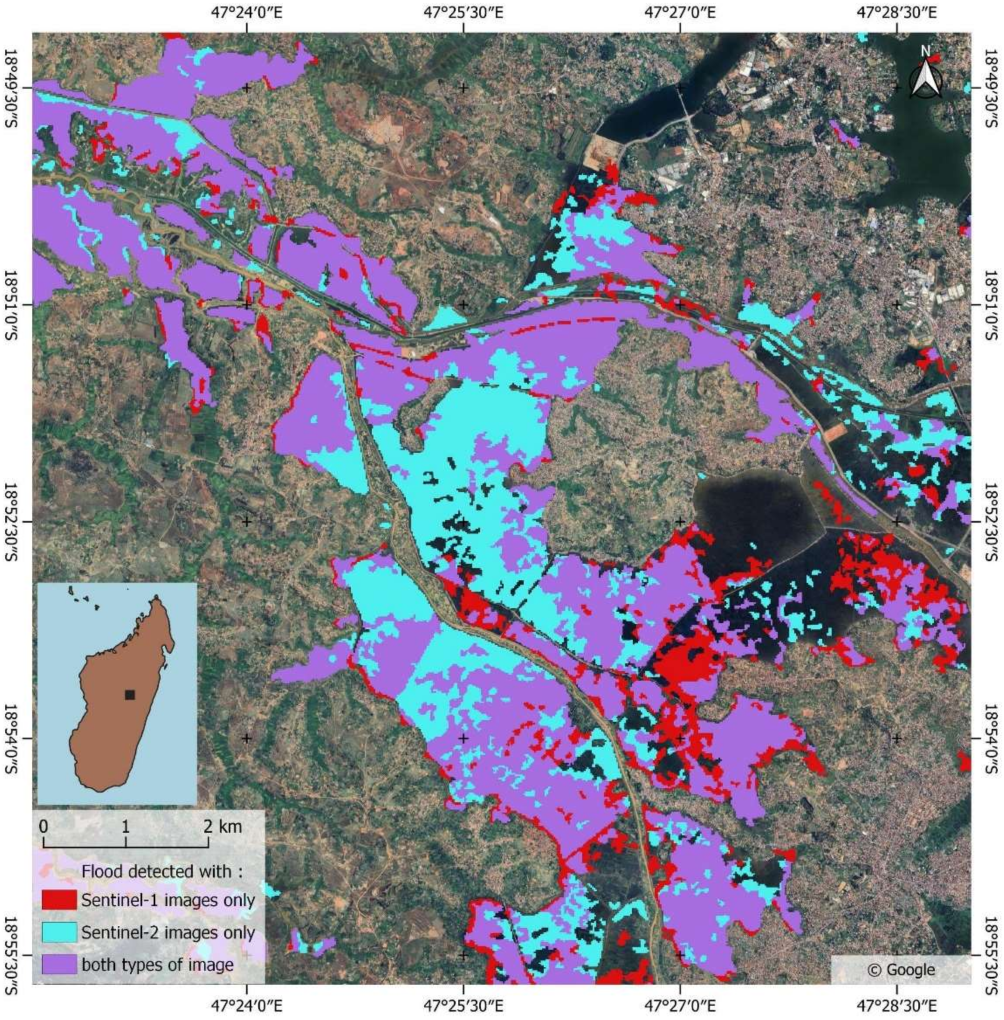

Figure 3. Map of floods detected around Antananarivo generated from Sentinel-1 and Sentinel-2. Optical images acquired 13 March 2018 and 18 September 2017 (reference). Radar images acquired 12 March 2018 and 18 September 2017 (reference).

For a more unbiased validation, 100 random points were generated for each class (flooded and non-flooded). Optical and radar images, along with water indices, were visually interpreted to establish the ground truth state of each point. This was carried out while considering the available information on flooding in the study area.

To achieve a more impartial validation process, a set of 100 random points was meticulously generated for each class, distinguishing between areas affected by flooding and those unaffected (flooded and non-flooded, respectively). Subsequently, a comprehensive analysis of optical and radar images, along with water index, was conducted using a visual interpretation approach. This method allowed for the actual ground truth state of each point within the study area. This interpretation process was conducted with consideration for the available information regarding historical occurrences of flooding within the study area, ensuring a robust and reliable validation process.

3. Results

3.1. Calibration phase

The processing chain is calibrated on the outskirts of Antananarivo by comparing results with those obtained from two optical images (pre- and post-flood).

Figure 3 shows surface water detected from Sentinel-2 optical imagery with automatic thresholding of the normalized difference water index (NDWI). Permanent water bodies are filtered out by processing another Sentinel-2 image acquired on 18 September 2017 (dry season) in the same fashion. This date was chosen because a Sentinel-1 image acquired the same day will be used as the reference radar image when processing radar data.

Figure 4 shows flood-detection results obtained using a single polarization (VV, and then VH) and both polarizations at the same time.

The calibration area experiences recurrent flooding events. Taking into account historical flood patterns, a threshold of -0.35 is used.

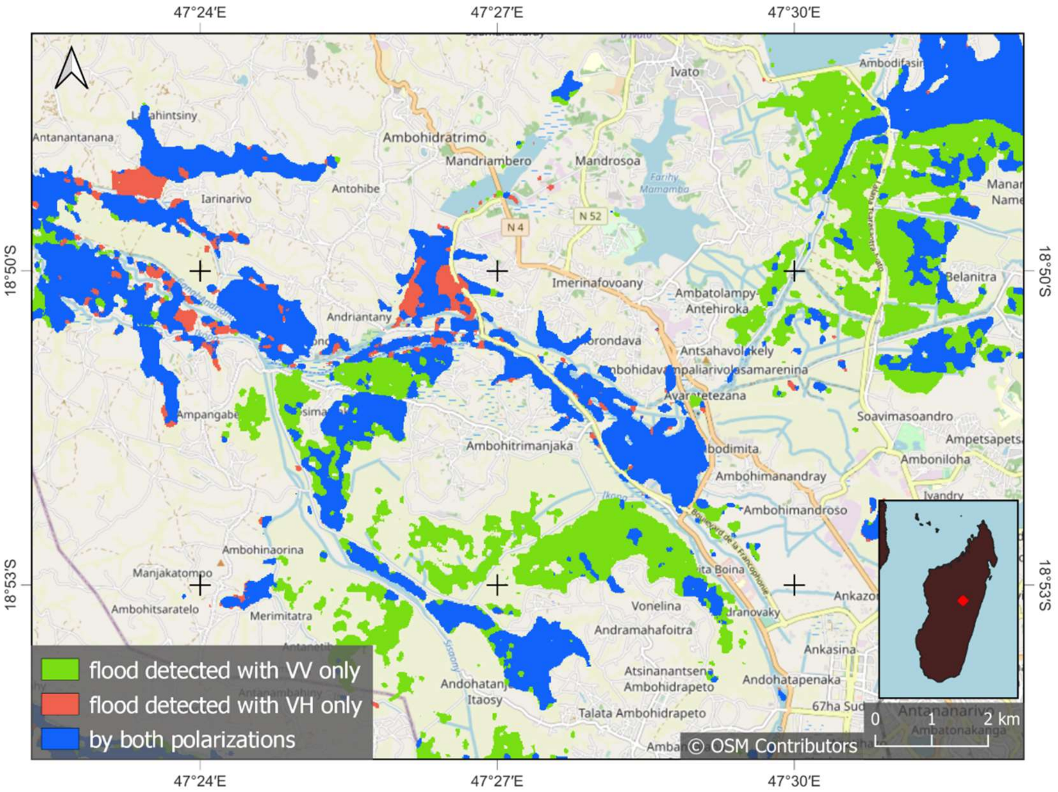

Figure 4. Detection of floods in the Antananarivo plain using different polarizations of the Sentinel-1 image (VV only, VH only and both VV and VH). The post-flood image was acquired on 13 March 2018 and the reference image on 18 September 2017.

We note that flood-detection results obtained with the two polarizations are complementary, confirming the findings of Clément *et al.* [13]. Both polarizations will therefore be used henceforth.

Table 1 shows how processing chain results match according to the type of filter used with respect to the result obtained with two Sentinel-2 optical images. The figures indicate the percentage of ‘flood’ pixels simultaneously identified by both approaches (optical and radar).

Table 1. Agreement of processing chain results according to the type of filter used by comparing with the result obtained from Sentinel-2 optical images.

Filter	Mono[1] (%)	Multi[2] (%)
No filter	92.45	--
BOXCAR	92.83	92.77
Gamma MAP	92.68	92.64
LEE	92.76	92.70
LEE SIGMA	92.73	92.67
REFINED LEE	93.24	93.12

[1] Processing with post-flood image and a single reference image; [2] Processing with post-flood image and all available pre-flood images and applying multidate filters [55].

The best match is obtained with the Refined Lee filter on a single image. We note that accuracy is slightly reduced when using multidate filters. This may be because different non-permanent features (temporary water bodies) are in different places and have different shapes in the multidate imagery.

After generating 100 random points for each class (flood/non-flood), the real state of each pixel was verified manually. The confusion matrix is presented in Table 2, indicating an overall accuracy of 85%

Table 2. Confusion matrix of results of the flood detection in Antananarivo.

Predicted	**Reference**		
	non flood	**flood**	**Total**
non flood	92	8	100
flood	22	78	100
Total	114	86	200
Overall accuracy:	85 %		

3.2. Application for large-scale area

The processing chain is applied to identify flooded areas across the entire Madagascar island, covering an extensive area of 587,041 square kilometers for the 12 days following the passage of the cyclone Batsirai on 5 and 6 February 2022. We utilized both VV and VH polarizations with a spatial resolution of 20 meters and applied a Refined Lee filter to the images. We obtained 30 scenes covering Madagascar in its entirety.

For reference, we used a series of images acquired annually during the same 12 days period in previous years. 6 or 7 reference images were accessible for each scene. By combining the series of flood detection by majority vote, each pixel was considered flooded if it emerged in more than three of the reference images. Frequent submersions are thus excluded from the flood detection results.

To efficiently process the 30 scenes, we simultaneously submitted requests to Google Earth Engine (GEE) from the Google Colab session executing our Python code. GEE, equipped with automated resource allocation, managed concurrent processing seamlessly. Remarkably, all requests were completed in under an hour. The entire processing chain, from data processing to result visualization, was implemented within a single Colab session [52].

Figure 5 shows the flood-detection results for Cyclone Batsirai in Madagascar.

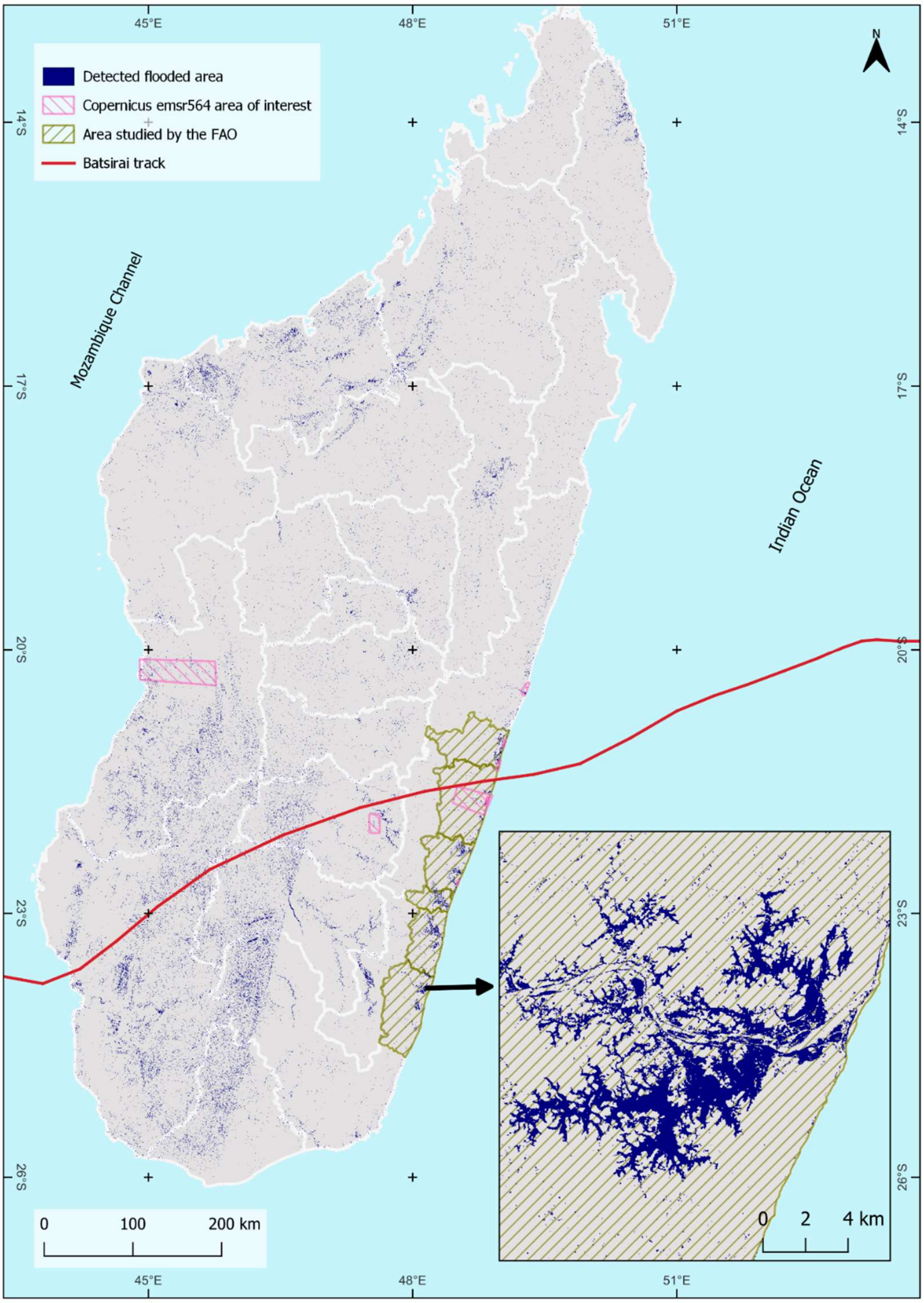

Figure 5. Flood Map of Madagascar During the 12-Day Period Following Cyclone Batsirai generated from the processing chain in GEE. Post event images were acquired from 5 to 17 February 2022.The enlarged area shows the district of Vangaindrano. The red line is the track of the cyclone.

3.3. Comparison with other flood mapping products

Figure 6 overlays the results obtained with the processing chain proposed here on the map supplied by Copernicus emrs564. This map shows the southeast region of Madagascar, which was hardest hit by Cyclone Batsirai. The images used for this study were acquired on 9 February 2022, i.e. three days after the floods peaked. Areas that initially were flooded may thus have changed status, which may explain why areas under water are underestimated with respect to the Copernicus product, generated from a Terrasar-X image of 6 February 2022.

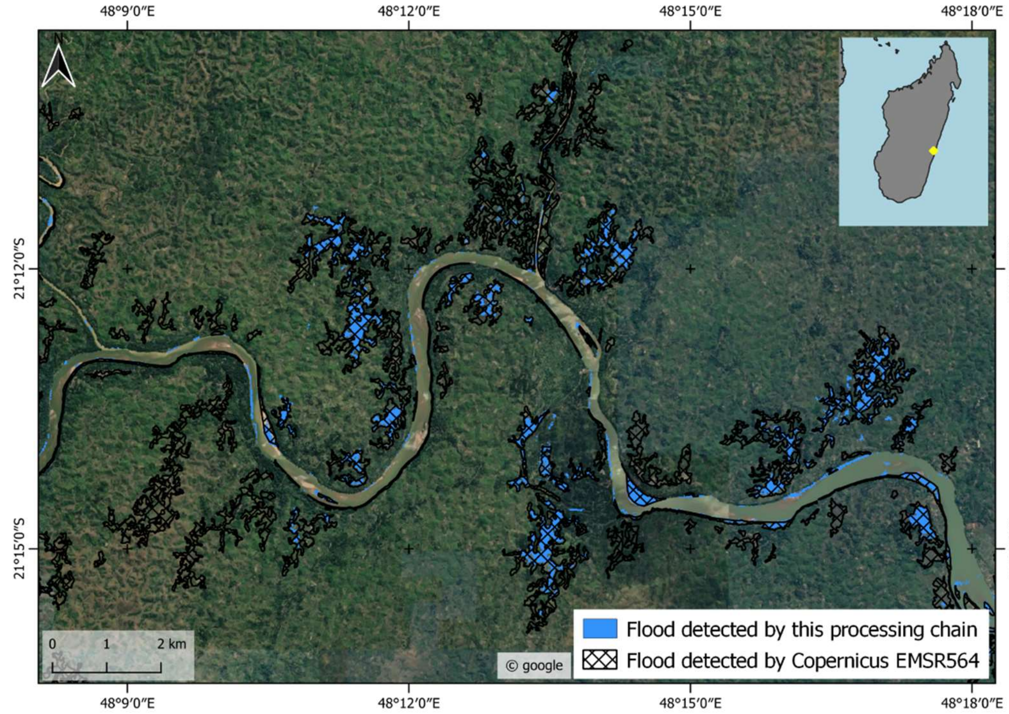

Figure 6. Flood map obtained with the processing chain overlaid on a flood map supplied by Copernicus emsr564 in the district of Mananjary. In blue are flooded areas detected by the processing chain generated by using Sentinel 1 image acquired on 9 February 2022. EMSR product is derived from TerraSAR-X image acquired on 6 February 2022.

The results again identified persistent flooding that represents a long-term vulnerability, especially where crop fields are affected. Such information can be of value during the post-flood recovery phase. Availability of Sentinel-1 imagery is an issue that may preclude timely application of this methodology, even more so now that Sentinel-1B is no longer in service. As Sentinel-1A is not retaskable, images may take several days to arrive (up to 16 days). The results are also compared with those obtained by the S1Chain developed by Alexandre *et al.* [34] (Figure 7). They are in close agreement, with a kappa value of 0.78. However, differences are observed in several small flooded areas. These differences may be due to filtering effects, since the two chains apply speckle filtering at different times. In S1Chain, this step is performed before terrain correction, whereas in GEE images have already been corrected for terrain effects before being posted online.

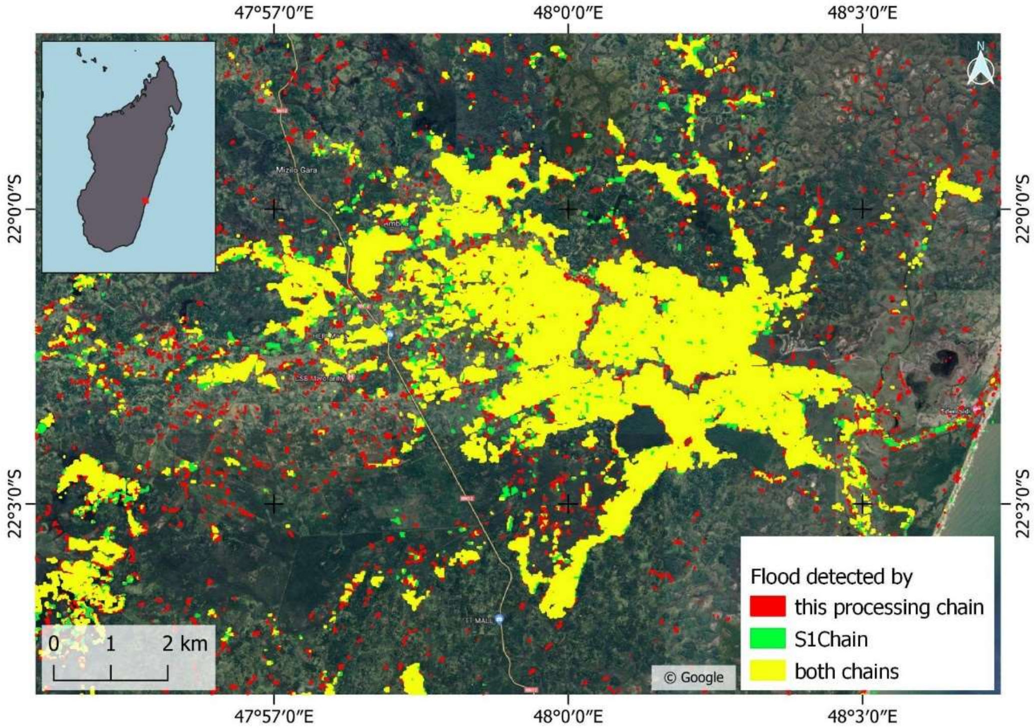

Figure 7. Comparison of floods detected with processing chain and S1Chain [49]. ***Backgound : Google satellite.***

3.4. Example applications

Statistics can be supplied quickly to emergency responders after cross-referencing these results with land cover maps produced by ESA and with OpenStreetMap products (Table 3). Likewise, they can be cross-referenced with built-up area data (Google Open Buildings) in GEE (Figure 8). 42.175 buildings were flooded.

Table 3. Flooded area according to type of land cover in ESA landcover and Open Street Map.

Land cover	Area (ha)
Shrubland	154.192
Herbaceous vegetation	582.599
Cultivated and managed vegetation/cropland	202.806
Bare/sparse vegetation	8.735
Forest	206.249

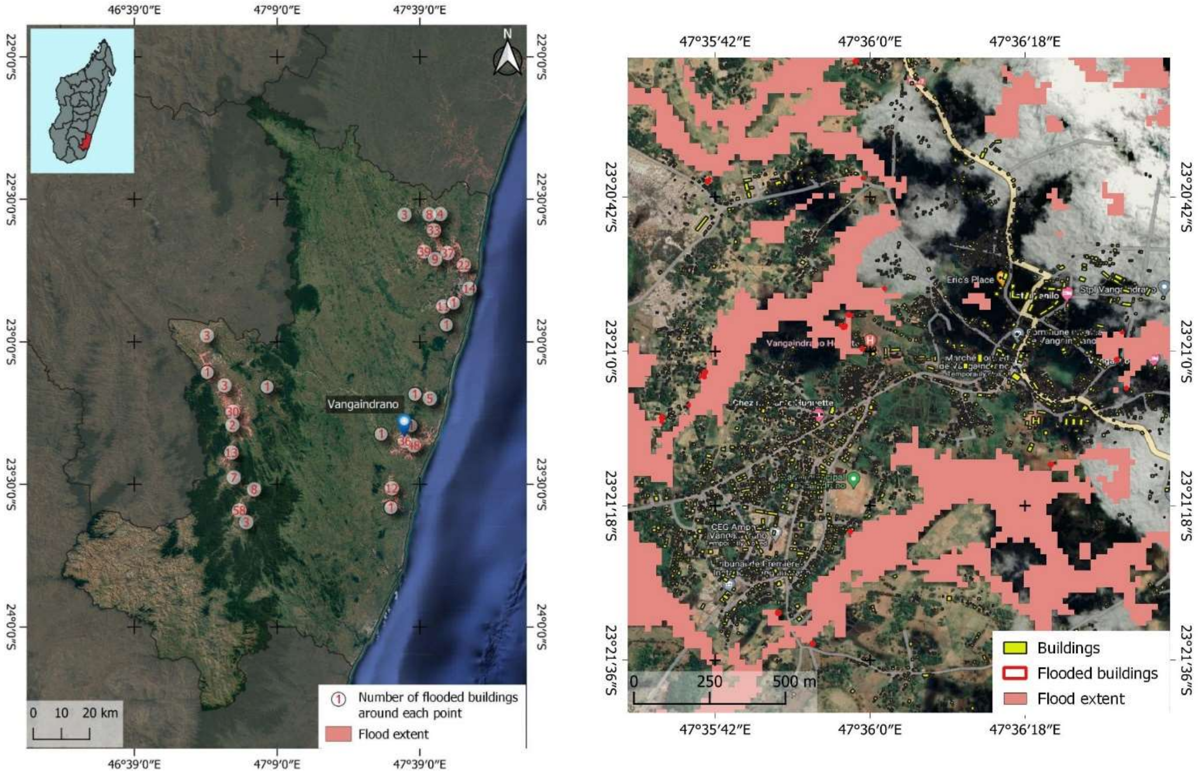

(**a**) (**b**)

Figure 8. **(a)** Map of flooded buildings after the passage of Cyclone Batsirai in the region of Atsimo Atsinanana. Buildings are from Google Open Buildings data available at [56]. (**b**) The enlarged area shows the city of Vangaindrano.

4. Discussion

In this study, the use of GEE has proven to be particularly relevant and effective in addressing the needs of this research. GEE provided easy access to preprocessed SAR data and computational resources, facilitating a two-fold study: firstly, characterizing the spatiotemporal distribution of water resources in Madagascar, including seasonal and inter-annual dynamics of water bodies, and secondly, assessing the impacts of flood events resulting from cyclones in operational mode to enhance decision-making using Earth observation products.

The results show that several locations affected by flooding during the passage of Cyclone Batsirai were not mapped by traditional emergency services, thus demonstrating the value of this new processing chain able to systematically generate flood maps for cyclone events on the scale of an entire country. The maps used by national emergency management agencies, obtained from various sources including through activation of the International Charter Space and Major Disasters, currently remain very limited in space and time. New information provided by our processing chain can help to improve disaster management and response.

However, it is worth noting that while GEE offers data availability and processing resources, including computational power and dedicated codes, which is particularly beneficial for territories like Madagascar with vast expanses and limited resources, certain limitations need to be considered. Sentinel-1 data comes preprocessed with limited flexibility for making specific adjustments. Additionally, there are restrictions on the volume of data that can be processed freely without subscribing. Ownership issues of developments can also be a concern, especially when collaborating with government agencies. Furthermore, the number of image processing tools and classification algorithms is limited to what is available in the API.

The approach of establishing continuous monitoring of the spatiotemporal distribution of water bodies and their evolution in Madagascar is particularly important for the operational application of mapping floods related to occasional cyclonic events. This continuous monitoring enables the provision of an updated reference map of water bodies, which can serve as a basis for all maps describing the extent of cyclonic floods. Therefore, the permanent availability of an up-to-date water reference product enhances the quality and speed of delivering cyclonic flood maps.

The differences observed between the products compared in Figures 7 and 8 can be explained in several ways. One of the main reasons lies in the temporal variations of image data, with each method using images acquired at different times. This temporal difference influences the characterization of floods, with the processing chain detecting floods at a specific time, while Copernicus EMS relies on older data, which impacts the results. Furthermore, the specific mapping methods and algorithms of each method are major sources of divergence. These divergences highlight the need for contextual analysis for accurate interpretation. The temporal complementarity between the approach focused on speed and extensive spatial coverage and official products, such as those from Copernicus, allows for a better understanding of flood evolution.

The approach developed stands out for its responsiveness and capacity to map the entire territory of Madagascar, whether for research purposes or operational applications in times of emergencies. This responsiveness holds considerable potential for improving flood response and disaster management.

The methodological developments of this flood detection tool with Google Earth Engine and Sentinel-1 radar imagery aim to meet operational needs during crises. This approach prioritizes the speed of impact map production and precision suitable for emergency situations rather than extreme accuracy. In a crisis situation, speed is crucial, and the goal is to obtain an overview of flooded areas for effective crisis management. This approach balances operational speed with sufficient precision for informed decision-making.

The contribution of our approach to flood management relies on the complementarity among various approaches, including those of Copernicus and the International Charter Space and Major Disasters. Sentinel-1 images are used for their ability to provide valuable information, even in unfavorable weather conditions. Our approach stands out for its speed, providing near-real-time data complementary to Copernicus products. The involvement of local stakeholders in data production and risk management enhances the capacity of communities to respond appropriately to floods. This collaboration contributes to more efficient flood management and rapid response in times of disaster. Furthermore, the utilization of Google Colab significantly eases collaboration. The processing chain is easily shareable, requiring no installation, and the Python notebook contains both code and formatted text, facilitating comprehension. This seamless integration of collaborative tools enhances the accessibility of our approach, promoting wider engagement and cooperation among stakeholders in addressing flood-related challenges.

5. Conclusions

This study developed a processing chain to identify flooded areas using radar imagery in Google Earth Engine. The chain was developed in Google Colab in the form of a Python notebook. We have shown that our processing chain is effective in detecting flooded areas throughout Madagascar. This processing over large areas was possible thanks to the computing power and the rapid access to the data offered by Google Earth Engine. The GEE platform is a real opportunity for work on large volumes of data, particularly for countries like Madagascar where bandwidth and the Internet network can be quite inconsistent.

The results show that several locations affected by flooding during the passage of Cyclone Batsirai were not mapped by traditional emergency mapping services, thus demonstrating the value of systematically generating national flood maps for cyclone events. The maps used by national emergency management agencies, obtained from various sources including through activation of the International Charter Space and Major Disasters, currently remain very limited. New information provided by our processing chain can help to improve disaster management and response.

Cyclonic seasons give rise to clouds and atmospheric disturbances. Less affected than optical imagery, we have shown that radar Sentinel-1 data is a reliable solution for detecting flooding during these periods. It makes sense to continue working on this data, since ESA has announced the launch of Sentinel 1-C this year, and the rest of the programme is already planned. Building processing chains and operational tools based on sentinel 1 data is part of a long-term vision.

Code from the processing chain could easily be adapted to use radar images from other satellites and replace Sentinel-1 imagery when it is not available. The chain currently runs on Google Earth Engine. Adapting the script to work with multiple backends such as Digital Earth Africa [57] or Microsoft Planetary Computer [58] or other proposals like ESA's [59] would be very interesting.

Author Contributions: Conceptualization, R.J., C.R. and S. R.; methodology, R. J., T.C., Sa.R. and S. R.; software, R. J.; T. C., and P. M.; validation, R. J., C. R. and T. C.; formal analysis, R. J.; investigation, R. J.; resources, R. J.; data curation, R. J.; writing—original draft preparation, R. J.; writing—review and editing, R. J., C. R., C.A., T.C., P. M., G. P. and S.R.; visualization, R. J.; supervision, G.P., S.R., Sa. R; project administration, G. P.; funding acquisition, C. R., G. P. All authors have read and agreed to the published version of the manuscript.

Funding: This work is supported by the EU Interreg project Renovrisk-Impact funded by the European Union, the IRD, and Reunion Regional Council.

Data Availability Statement: Python code is available freely by following this link https://github.com/johrosa/ls-FloodMonitoring/blob/main/country_scale_flood_detection.ipynb.

Conflicts of Interest: The authors declare no conflict of interest.

References

1. IPCC Climate Change 2021: The Physical Basis Available online: https://www.ipcc.ch/report/ar6/wg1/ (accessed on 1 August 2022).
2. Guha-Sapir, D.; Hargitt, D.; Hoyois, P. *Thirty Years of Natural Disasters 1974 - 2003: The Number*; UCL Presses Universitaires de Louvain [u.a.]: Louvain, 2004; ISBN 978-2-930344-71-3.
3. McDermott, T.K.J. Global Exposure to Flood Risk and Poverty. *Nat Commun* **2022**, *13*, 3529, doi:10.1038/s41467-022-30725-6.
4. Otto, F.E.L.; Zachariah, M.; Wolski, P.; Pinto, I.; Nhamtumbo, B.; Bonnet, R.; Vautard, R.; Philip, S.; Kew, S.; Luu, L.N.; *et al. Climate Change Increased Rainfall Associated with Tropical Cyclones Hitting Highly Vulnerable Communities in Madagascar, Mozambique & Malawi*; 2022; p. 41;.
5. Fitchett, J.M. Recent Emergence of CAT5 Tropical Cyclones in the South Indian Ocean. *South African Journal of Science* **2018**, *114*, doi:10.17159/sajs.2018/4426.
6. Ramiaramanana, F.N.; Teller, J. Urbanization and Floods in Sub-Saharan Africa: Spatiotemporal Study and Analysis of Vulnerability Factors—Case of Antananarivo Agglomeration (Madagascar). *Water* **2021**, *13*, 149, doi:10.3390/w13020149.
7. Ajmar, A.; Boccardo, P.; Broglia, M.; Kucera, J.; Giulio-Tonolo, F.; Wania, A. Flood Damage Survey and Assessment: New Insights from Research and Practice. In *Response to flood events: the role of satellite-based emergency mapping and the experience of the Copernicus Emergency Management Service*; Daniela Molinari, F.B., Scira Menoni, Ed.; John Wiley & Sons, Inc., 2017; Vol. 228, pp. 213–228 ISBN 978-1-119-21792-3.
8. Wania, A.; Joubert-Boitat, I.; Dottori, F.; Kalas, M.; Salamon, P. Increasing Timeliness of Satellite-Based Flood Mapping Using Early Warning Systems in the Copernicus Emergency Management Service. *Remote Sensing* **2021**, *13*, 2114, doi:10.3390/rs13112114.
9. International Disasters Charter Available online: https://disasterscharter.org/en/web/guest/home (accessed on 2 June 2023).
10. FAO *Madagascar: Évaluation des dommages et des pertes causés par les cyclones Batsirai et Emnati sur le secteur agricole dans le Grand Sud-Est de Madagascar : Rapport DIEM-impact, juin 2022*; FAO: Rome, Italy, 2022; ISBN 978-92-5-136561-8.
11. Biggin, D.S.; Blyth, K. A Comparison of ERS-1 Satellite Radar and Aerial Photography for River Flood Mapping. *Water and Environment Journal* **1996**, *10*, 59–64, doi:10.1111/j.1747-6593.1996.tb00009.x.
12. Rochon, G.; Bonn, F. *Précis de télédétection. Volume 1, Principes et méthodes*; 1992; Vol. 1;.
13. Carreño Conde, F.; De Mata Muñoz, M. Flood Monitoring Based on the Study of Sentinel-1 SAR Images: The Ebro River Case Study. *Water* **2019**, *11*, 2454, doi:10.3390/w11122454.
14. Clement, M.A.; Kilsby, C.G.; Moore, P. Multi-Temporal Synthetic Aperture Radar Flood Mapping Using Change Detection: Multi-Temporal SAR Flood Mapping Using Change Detection. *Journal of Flood Risk Management* **2018**, *11*, 152–168, doi:10.1111/jfr3.12303.

15. Rahman, Md.R.; Thakur, P.K. Detecting, Mapping and Analysing of Flood Water Propagation Using Synthetic Aperture Radar (SAR) Satellite Data and GIS: A Case Study from the Kendrapara District of Orissa State of India. *The Egyptian Journal of Remote Sensing and Space Science* **2018**, *21*, S37–S41, doi:10.1016/j.ejrs.2017.10.002.
16. Baghdadi, N.; King, C.; Bourguignon, A.; Remond, A. Potential of ERS and Radarsat Data for Surface Roughness Monitoring over Bare Agricultural Fields: Application to Catchments in Northern France. *International Journal of Remote Sensing* **2002**, *23*, 3427–3442, doi:10.1080/01431160110110974.
17. Amitrano, D.; Martino, G.D.; Iodice, A.; Ruello, G. Unsupervised Rapid Flood Mapping Using Sentinel-1 GRD SAR Images. *IEEE TRANSACTIONS ON GEOSCIENCE AND REMOTE SENSING* 10.
18. Li, Y.; Martinis, S.; Plank, S.; Ludwig, R. An Automatic Change Detection Approach for Rapid Flood Mapping in Sentinel-1 SAR Data. *International Journal of Applied Earth Observation and Geoinformation* **2018**, *73*, 123–135, doi:10.1016/j.jag.2018.05.023.
19. Lu, D.; Mausel, P.; Brondízio, E.; Moran, E. Change Detection Techniques. *International Journal of Remote Sensing* **2004**, *25*, 2365–2401, doi:10.1080/0143116031000139863.
20. Singh, A. Review Article Digital Change Detection Techniques Using Remotely-Sensed Data. *International Journal of Remote* 21. Weismiller, R.A.; Kristof, S.J.; Scholz, D.K.; Anuta, P.E.; Momin, S.A. Change Detection in Coastal Zone Environments. *Photogrammetric Engineering and Remote Sensing* **1977**, *43*, 1533–1539.
21. Zhang, Y.; Wang, S.; Wang, C.; Li, J.; Zhang, H. SAR Image Change Detection Using Saliency Extraction and Shearlet Transform. *IEEE Journal of Selected Topics in Applied Earth Observations and Remote Sensing* **2018**, *11*, 4701–4710, doi:10.1109/JSTARS.2018.2866540.
22. Wan, L.; Zhang, T.; You, H. Object-Based Multiscale Method for SAR Image Change Detection. *JARS* **2018**, *12*, 025004, doi:10.1117/1.JRS.12.025004.
23. Rignot, E.J.M.; van Zyl, J.J. Change Detection Techniques for ERS-1 SAR Data. *IEEE Transactions on Geoscience and Remote Sensing* **1993**, *31*, 896–906, doi:10.1109/36.239913.
24. Bayik, C.; Abdikan, S.; Ozbulak, G.; Alasag, T.; Aydemir, S.; Balik Sanli, F. Exploiting Multi-Temporal Sentinel-1 SAR Data for Flood Extend Mapping. *Int. Arch. Photogramm. Remote Sens. Spatial Inf. Sci.* **2018**, *XLII-3/W4*, 109–113, doi:10.5194/isprs-archives-XLII-3-W4-109-2018.
25. Chini, M.; Pelich, R.; Pulvirenti, L.; Pierdicca, N.; Hostache, R.; Matgen, P. Sentinel-1 InSAR Coherence to Detect Floodwater in Urban Areas: Houston and Hurricane Harvey as A Test Case. *Remote Sensing* **2019**, *11*, 107, doi:10.3390/rs11020107.
26. Samela, C.; Troy, T.J.; Manfreda, S. Geomorphic Classifiers for Flood-Prone Areas Delineation for Data-Scarce Environments. *Advances in Water Resources* **2017**, *102*, 13–28, doi:10.1016/j.advwatres.2017.01.007.
27. Rennó, C.D.; Nobre, A.D.; Cuartas, L.A.; Soares, J.V.; Hodnett, M.G.; Tomasella, J.; Waterloo, M.J. HAND, a New Terrain Descriptor Using SRTM-DEM: Mapping Terra-Firme Rainforest Environments in Amazonia. *Remote Sensing of Environment* **2008**, *112*, 3469–3481, doi:10.1016/j.rse.2008.03.018.
28. Razafipahatelo, D.; Rakotoniaina, S.; Rakotondraompiana, S. Automatic Floods Detection with a Kernel K-Means Approach. In Proceedings of the 2014 IEEE Canada International Humanitarian Technology Conference - (IHTC); June 2014; pp. 1–4.
29. Gorelick, N.; Hancher, M.; Dixon, M.; Ilyushchenko, S.; Thau, D.; Moore, R. Google Earth Engine: Planetary-Scale Geospatial Analysis for Everyone. *Remote Sensing of Environment* **2017**, *202*, 18–27, doi:10.1016/j.rse.2017.06.031.
30. Mutanga, O.; Kumar, L. Google Earth Engine Applications. *Remote Sensing* **2019**, *11*, 591, doi:10.3390/rs11050591.
31. DeVries, B.; Huang, C.; Armston, J.; Huang, W.; Jones, J.W.; Lang, M.W. Rapid and Robust Monitoring of Flood Events Using Sentinel-1 and Landsat Data on the Google Earth Engine. *Remote Sensing of Environment* **2020**, *240*, 111664, doi:10.1016/j.rse.2020.111664.
32. Moharrami, M.; Javanbakht, M.; Attarchi, S. Automatic Flood Detection Using Sentinel-1 Images on the Google Earth Engine. *Environ Monit Assess* **2021**, *193*, 248, doi:10.1007/s10661-021-09037-7.
33. Alexandre, C.; Johary, R.; Catry, T.; Mouquet, P.; Révillion, C.; Rakotondraompiana, S.; Pennober, G. A Sentinel-1 Based Processing Chain for Detection of Cyclonic Flood Impacts. *Remote Sensing* **2020**, *12*, 252, doi:10.3390/rs12020252.
34. National Centers for Environmental Information (NCEI) Available online: https://www.ncei.noaa.gov/ (accessed on 13 July 2023).
35. Sentinel-1 - Missions - Sentinel Online Available online: https://copernicus.eu/missions/sentinel-1 (accessed on 1 June 2023).
36. Sentinel-1 SAR GRD: C-Band Synthetic Aperture Radar Ground Range Detected, Log Scaling | Earth Engine Data Catalog | Google for Developers Available online: https://developers.google.com/earth-engine/datasets/catalog/COPERNICUS_S1_GRD (accessed on 31 May 2023).

37. Scale | Google Earth Engine Available online: https://developers.google.com/earth-engine/guides/scale (accessed on 18 November 2022).
38. McFeeters, S.K. The Use of the Normalized Difference Water Index (NDWI) in the Delineation of Open Water Features. *International Journal of Remote Sensing* **1996**, *17*, 1425–1432, doi:10.1080/01431169608948714.
39. Stathopoulos, N.; Kalogeropoulos, K.; Polykretis, C.; Skrimizeas, P.; Louka, P..; Efthimios, K.; Chalkias C. Introducing Flood Susceptibility Index Using Remote-Sensing Data and Geographic Information Systems: Empirical Analysis in Sperchios River Basin, Greece. In *Remote Sensing of Hydrometeorological Hazards*; CRC Press, 2017 ISBN 978-1-315-15494-7
40. Zanaga, D., Van De Kerchove, R., Daems, D., De Keersmaecker, W., Brockmann, C., Kirches, G., Wevers, J., Cartus, O., Santoro, M., Fritz, S., Lesiv, M., Herold, M., Tsendbazar, N.E., Xu, P., Ramoino, F., Arino, O., 2022. ESA WorldCover 10 m 2021 v200. https://doi.org/10.5281/zenodo.7254221
41. Helbich, M., Amelunxen, C., Neis, P., & Zipf, A. (2012). Comparative spatial analysis of positional accuracy of OpenStreetMap and proprietary geodata. Proceedings of GI_Forum, 4, 24.
42. Sirko, W.; Kashubin, S.; Ritter, M.; Annkah, A.; Bouchareb, Y.S.E.; Dauphin, Y.; Keysers, D.; Neumann, M.; Cisse, M.; Quinn, J. Continental-Scale Building Detection from High Resolution Satellite Imagery 2021. https://doi.org/10.48550/arXiv.2107.12283
43.
44. Donchyts, G.; Winsemius, H.; Schellekens, J.; Erickson, T.; Gao, H.; Savenije, H.; van de Giesen, N. *Global 30m Height Above the Nearest Drainage*; 2016;
45. Digital Elevation Data - with SRTM Voids Filled Using Accurate Topographic Mapping Available online: http://viewfinderpanoramas.org/dem3.html (accessed on 5 June 2023).
46. Mullissa, A.; Vollrath, A.; Odongo-Braun, C.; Slagter, B.; Balling, J.; Gou, Y.; Gorelick, N.; Reiche, J. Sentinel-1 SAR Backscatter Analysis Ready Data Preparation in Google Earth Engine. *Remote Sensing* **2021**, *13*, 1954, doi:10.3390/rs13101954.
47. Di Martino, G.; Poderico, M.; Poggi, G.; Riccio, D.; Verdoliva, L. Benchmarking Framework for SAR Despeckling. *IEEE Trans. Geosci. Remote Sensing* **2014**, *52*, 1596–1615, doi:10.1109/TGRS.2013.2252907.
48. Mascarenhas, N.D.A. An Overview of Speckle Noise Filtering in SAR Images. **1997**, *407*, 71.
49. Lopes, A.; Nezry, E.; Touzi, R.; Laur, H. Maximum A Posteriori Speckle Filtering And First Order Texture Models In Sar Images. In Proceedings of the 10th Annual International Symposium on Geoscience and Remote Sensing; May 1990; pp. 2409–2412.
50. Lee, J.-S. Digital Image Enhancement and Noise Filtering by Use of Local Statistics. *IEEE Transactions on Pattern Analysis and Machine Intelligence* **1980**, *PAMI-2*, 165–168, doi:10.1109/TPAMI.1980.4766994.
51. Lee, J.-S.; Wen, J.-H.; Ainsworth, T.L.; Chen, K.-S.; Chen, A.J. Improved Sigma Filter for Speckle Filtering of SAR Imagery. *IEEE Transactions on Geoscience and Remote Sensing* **2009**, *47*, 202–213, doi:10.1109/TGRS.2008.2002881.
52. Lee, J.-S.; Grunes, M.R.; Grandi, G. de Polarimetric SAR Speckle Filtering and Its Implication for Classification. *IEEE Transactions on Geoscience and Remote Sensing* **1999**, *37*, 2363–2373, doi:10.1109/36.789635.
53. Coppin, P.R.; Bauer, M.E. Processing of Multitemporal Landsat TM Imagery to Optimize Extraction of Forest Cover Change Features. *IEEE Trans. Geosci. Remote Sensing* **1994**, *32*, 918–927, doi:10.1109/36.298020.
54. Gianinetto, M.; Villa, P. Mapping Hurricane Katrina's Widespread Destruction in New Orleans Using Multisensor Data and the Normalized Difference Change Detection (NDCD) Technique. *International Journal of Remote Sensing* **2011**, *32*, 1961–1982, doi:10.1080/01431161003645808.
55. Google Colab Available online: https://research.google.com/colaboratory/faq.html?hl=fr (accessed on 15 May 2023).
56. Open Buildings Available online: https://sites.research.google/open-buildings/ (accessed on 13 July 2023).
57. Welcome to Digital Earth Africa | Digital Earth Africa Available online: https://www.digitalearthafrica.org/ (accessed on 31 May 2023).
58. Microsoft Planetary Computer Available online: https://planetarycomputer.microsoft.com/ (accessed on 31 May 2023).
59. Network Of Resources Available online: https://eo4society.esa.int/network-of-resources/ (accessed on 31 May 2023).